

Advanced magneto-acousto-electrical tomography based on circular arrays of omnidirectional transducers and orthogonally oriented electrodes

Peixia Li(李培霞), Wei Chen(陈伟), Hao Qian(钱昊), Yulong Zhou(周瑜龙), Gepu Guo(郭各朴), Juan Tu(屠娟), Dong Zhang(章东), and Qingyu Ma(马青玉)

Citation: Chin. Phys. B, 2026, 35 (**5**): 054302. DOI: 10.1088/1674-1056/ae089a
http://cpb.iphy.ac.cn; http://iopscience.iop.org/cpb

What follows is a list of articles you may be interested in

Nonlinear inversion of ultrasonic guided waves for *in vivo* evaluation of cortical bone properties

Xiaojun Song(宋小军), Tiandi Fan(樊天地), Jundong Zeng(曾俊冬), Qin-Zhen Shi(石勤振), Qiong Huang(黄琼), Meilin Gu(顾美琳), Petro Moilanen, Yi-Fang Li(李义方), and Dean Ta(他得安)

Chin. Phys. B, 2022, 31 (**7**): 074301. DOI: 10.1088/1674-1056/ac3eca

Deep learning for image reconstruction in thermoacoustic tomography

Qiwen Xu(徐启文), Zhu Zheng(郑铸), and Huabei Jiang(蒋华北)

Chin. Phys. B, 2022, 31 (**2**): 024302. DOI: 10.1088/1674-1056/ac0dab

Performance improvement of magneto-acousto-electrical tomography for biological tissues with sinusoid-Barker coded excitation

Zheng-Feng Yu(余正风), Yan Zhou(周奘), Yu-Zhi Li(李禹志), Qing-Yu Ma(马青玉), Ge-Pu Guo(郭各朴), Juan Tu(屠娟), Dong Zhang(章东)

Chin. Phys. B, 2018, 27 (**9**): 094302. DOI: 10.1088/1674-1056/27/9/094302

Lorentz force electrical impedance tomography using pulse compression technique

Zhi-shen Sun(孙直申), Guo-qiang Liu(刘国强), Hui Xia(夏慧)

Chin. Phys. B, 2017, 26 (**12**): 124302. DOI: 10.1088/1674-1056/26/12/124302

Conductivity reconstruction algorithms and numerical simulations for magneto-acousto-electrical tomography with piston transducer in scan mode

Guo Liang (郭亮), Liu Guo-Qiang (刘国强), Xia Hui (夏慧), Liu Yu (刘宇), Lu Min-Hua (陆敏华)

Chin. Phys. B, 2014, 23 (**10**): 104303. DOI: 10.1088/1674-1056/23/10/104303

Advanced magneto-acousto-electrical tomography based on circular arrays of omnidirectional transducers and orthogonally oriented electrodes

Peixia Li(李培霞)[1], Wei Chen(陈伟)[1], Hao Qian(钱昊)[1], Yulong Zhou(周瑜龙)[2], Gepu Guo(郭各朴)[1,†], Juan Tu(屠娟)[3], Dong Zhang(章东)[3], and Qingyu Ma(马青玉)[1,‡]

[1] *School of Computer and Electronic Information, Nanjing Normal University, Nanjing* 210023, *China*
[2] *School of Information Engineering, Taizhou College, Nanjing Normal University, Taizhou* 225300, *China*
[3] *Institute of Acoustics, Nanjing University, Nanjing* 210093, *China*

(Received 21 August 2025; revised manuscript received 14 September 2025; accepted manuscript online 18 September 2025)

Magneto-acousto-electrical tomography (MAET) is a promising imaging modality capable of visualizing electrical conductivity variations in tissues. However, its imaging quality and efficiency are often compromised by the mechanical rotation and scanning processes. An advanced MAET approach that employs cyclic excitation of omnidirectional transducers and synchronous detection with orthogonally oriented electrodes is presented. The principle of MAE measurement regarding acoustic excitation and electrical detection at arbitrary positions is derived. It confirms that the signal attenuation originates from the cosine product of the angles between the conductivity boundary and the positions of the transducer and electrode. A new tomographic algorithm utilizing amplitude summation for electrodedetected signals is developed, and it is further refined through the application of square-amplitude summation for orthogonally oriented electrodes. The performance improvement is validated by accurate reconstruction of an eccentrically positioned cylindrical model, using an optimized experimental system comprising 32 sources and 4 electrodes. These promising results demonstrate that the efficiency, stability, and quality of MAET can be substantially enhanced through electrically controlled cyclic excitation and synchronous detection, thereby eliminating the need for mechanical activities. By integrating MAET with ultrasonic CT, a novel dual-modality imaging strategy that leverages both electrical and acoustic impedances can be further advanced.

Keywords: magneto-acousto-electrical tomography, omnidirectional sources, orthogonally oriented electrodes, image reconstruction algorithm, system optimization

PACS: 43.80.Ev, 72.55.+s, 73.50.Rb

DOI: 10.1088/1674-1056/ae089a **CSTR:** 32038.14.CPB.ae089a

1. Introduction

Tumor is a kind of disease that poses severe threats to human health. Conventional diagnostic techniques, including x-ray, ultrasound, and magnetic resonance imaging (MRI), have been utilized to detect and characterize the morphological, structural, and physicochemical alterations[1] in tissues. However, several issues, such as ionizing radiation damage, limited spatial resolution, and inadequate real-time capabilities, remain to be addressed. Previous studies have documented that the relative change in electrical impedance of tissues is significantly more pronounced than those in morphology or structure,[2–4] exceeding alterations in acoustic impedance by a factor of several-fold. This property establishes electrical impedance change as a sensitive parameter for early tumor diagnosis. Electrical impedance tomography (EIT),[5–7] magnetic induction tomography (MIT),[8–10] and magnetic resonance electrical impedance tomography (MREIT)[11–13] have been developed for imaging electrical impedance variations within biological tissues. However, their practical applications are still constrained by the limitations of high-current injection, tissue shielding effects, ill-posed nature of image reconstruction, slow imaging speed, and poor spatial resolution, and so on. By leveraging the coupling among magnetic, acoustic, and electronic fields,[14,15] magneto-acousto-electrical (MAE) technology[16,17] has been developed. MAE signals generate at conductivity boundaries through the interaction of acoustic vibrations with the magnetic field, containing essential information on boundary location and conductivity variation. MAE tomography (MAET) is free from the limitations of current injection and tissue insulation, thus holding significant potential for biomedical imaging, with the advantages of high contrast and spatial resolution.

Traditional B-mode MAE imaging was performed via linear scanning with either a planar or focused transducer, accompanied by signal detection using electrodes positioned perpendicular to the beam axis. Short-pulse[18–22] and coded excitations[23–28] were employed to enhance imaging depth while simultaneously improving axial resolution for layered

†Corresponding author. E-mail: guogepu@njnu.edu.cn
‡Corresponding author. E-mail: maqingyu@njnu.edu.cn

© 2026 Chinese Physical Society and IOP Publishing Ltd. All rights, including for text and data mining, AI training, and similar technologies, are reserved.

tissue models. Grasland-Mongrain *et al.* proposed the Lorentz force electrical impedance tomography[29] for the first time. They reconstructed conductivity gradient images for beef tissue and gel samples through acoustic focusing, and demonstrated a strong correlation between conductivity distributions and ultrasound images. A sinusoidal-Barker coded excitation was introduced by Yu *et al.* to enhance detection depth and signal-to-noise ratio (SNR) for MAE measurements,[23] with side lobes substantial suppressed by mismatch filtering. Li *et al.* detected both positive and negative MAE pulses emanating from conductivity boundaries of a mouse liver tumor model,[22] and reconstructed B-mode images of conductivity gradients. These studies indicate that high-quality images can only be reconstructed for layered tissues, in which the boundaries are oriented perpendicular to the beam axis. However, due to the potential signal attenuation caused by inclined acoustic incidence,[22] achieving accurate MAE imaging for objects of arbitrary shapes remains a significant challenge.

Experimental results have demonstrated that the MAE signal attenuation can be reduced by optimizing the incident direction, ensuring accurate vertical alignment between the acoustic beam and the conductivity boundaries. As a result, a tomographic approach based on rotation and scanning[30] was introduced into MAE imaging. This method effectively mitigates signal attenuations occurring at tissue boundaries through multi-angle linear scanning and enables MAET reconstruction of conductivity boundaries for arbitrarily shaped tissues via rotational synthesis of B-mode images. Sun *et al.* performed MAE imaging using linear scanning with a focused transducer and reconstructed MAET images at 5° rotational increments.[31] However, the imaging accuracy might be compromised by the non-uniform pressure distribution within the focal region. To accelerate MAET imaging, Sun *et al.* developed MAE computed tomography utilizing multi-angle plane wave excitation.[32–34] Due to the possible inadequate beam coverage across the entire object, a small rotation angle was necessary. Li *et al.* proposed a general principle[35] of MAET for objects of arbitrary shapes, taking into account the radiation pattern of actual transducers and the direction of conductivity boundaries. An optimized MAET scheme utilizing a linear array of point sources was confirmed, enabling rapid imaging with a maximum rotation angle of 12°. Kunyansky *et al.* developed a rotational MAET scanner that employs a focused transducer and two pairs of electrodes,[30] and recovered images with 200 rotations and 40 linear scans. Nevertheless, the underlying mechanism of multi-electrode measurements has not yet been elucidated. Moreover, MAET continues to be limited by the substantial time required for mechanical rotation and scanning.

Despite advancements in recent years, several challenges remain to be addressed for MAET. The efficiency of B-mode imaging is severely compromised by the time-consuming mechanical scanning process. Although plane wave steering can accelerate linear scanning, the complexity and cost associated with multi-angle excitation based on phased array are significantly increased. Moreover, the use of two parallel electrodes can only detect the perpendicular components of MAE signals, while missing the components in the parallel direction. This limitation severely reduces the accuracy of MAE signal detection, thereby making it challenging to achieve high-precision imaging for inclined boundaries. In addition, the quality and efficiency of MAET imaging are restricted by the reduced stability introduced by mechanical scanning and rotation. Therefore, developing a new MAET approach that can be electronically controlled and is free from mechanical activities holds great significance in biomedical imaging.

In this study, an advanced MAET approach that employs cyclic excitation of omnidirectional sources and synchronous detection with orthogonally oriented electrodes is introduced. The principle of MAE measurements applicable to objects of arbitrary shapes is derived. By analyzing the positional influence of transducers and electrodes, a new MAET algorithm utilizing amplitude summation for electrode-detected signals is developed based on the inverse Radon transform. This algorithm is further refined using square-amplitude summation for signals detected by orthogonally oriented electrodes. Simulation results demonstrate that the boundary shape and continuity of MAET imaging are primarily determined by the numbers of transducers and electrodes, respectively, with the minimum requirements of 30 and 4. The signal accuracy is effectively enhanced through the application of 4 orthogonally oriented electrodes, regardless of their specific positions. Accurate MAET imaging is validated both theoretically and experimentally using an optimized system comprising 32 sources and 4 electrodes. These promising results demonstrate that the stability, efficiency, and quality of MAET imaging can be substantially enhanced, free of mechanical rotation and scanning. By integrating MAET with ultrasonic CT, a next-generation dual-modality strategy that concurrently leverages electrical and acoustic impedances may emerge, opening transformative avenues in biomedical applications.

2. Principle and method

The schematic of MAET utilizing circular arrays of omnidirectional transducers and electrodes is illustrated in Fig. 1. An object of arbitrary shape with a conductivity distribution $\sigma(\boldsymbol{r})$, is immersed in a coupling liquid with conductivity σ_0. This setup is placed within a static magnetic field $\boldsymbol{B} = B\boldsymbol{e}_x$, with $\boldsymbol{e}_x$ being the unit vector in the x-direction. M omnidirectional sources and N electrodes are uniformly distributed on a circumference of radius R_0. The spatial angle between adja-

cent sources is $\phi = 2\pi/M$. $\boldsymbol{r}_{Tm}$ and $\boldsymbol{r}_{En}$ denote the respective positions of the m-th transducer (T_m) and the n-th electrode (E_n). To simplify theoretical derivations, each transducer is assumed to be perfectly insulated from the surrounding medium. Acoustic scattering and reflection at the electrodes and field boundaries are neglected. The acoustic radiation from each source propagates along the corresponding radial direction, covering the entire circular field domain. The acoustic vibrations induce electrical currents within the conductive media, which propagate through the object and the surrounding medium and are eventually detected by the electrodes. This process generates N MAE signals, which encapsulate information regarding the positions and conductivity gradients of tissue boundaries. Consequently, by electronically cycling through the excitation of M transducers and conducting synchronous measurements with N electrodes, a total of $M \times N$ MAE signals are collected.

As depicted in Fig. 1, the omnidirectional acoustic radiation follows the half-space spherical pattern. The acoustic pressure at $\boldsymbol{r}$ generated by T_m centered at $\boldsymbol{r}_{Tm}$ is described by

$$p(\boldsymbol{r}_{Tm},\boldsymbol{r}) = \left(2\mathrm{j}\omega\rho a^2 u_0/R_{Tm}\right)\exp\left[\mathrm{j}\left(\omega t - kR_{Tm}\right)\right], \quad (1)$$

where u_0 is the particle velocity on each source surface, a is the source radius. $k = \omega/c$ is the wavenumber, with ω being the angular frequency. ρ and c are the density and sound speed of the surrounding medium, respectively. $R_{Tm}=|\boldsymbol{r}-\boldsymbol{r}_{Tm}|$ is the distance between $\boldsymbol{r}_{Tm}$ and $\boldsymbol{r}$, with $t = R_{Tm}/c$. The angle β between the acoustic ray $I(\beta)(\boldsymbol{r}\boldsymbol{r}_{Tm})$ and the beam axis $(O\boldsymbol{r}_{Tm})$ lies within the range $[-\pi/2,\pi/2]$. The particle velocity $\boldsymbol{v}(\boldsymbol{r}_{Tm},\boldsymbol{r})$ is given by $\boldsymbol{v}(\boldsymbol{r}_{Tm},\boldsymbol{r}) = -(1/\rho)\int\nabla p(\boldsymbol{r}_{Tm},\boldsymbol{r})\,\mathrm{d}t$, with $\boldsymbol{e}_v = (\boldsymbol{r}-\boldsymbol{r}_{Tm})/|\boldsymbol{r}-\boldsymbol{r}_{Tm}|$ and ∇ being the gradient operator. Hence, the current density $\boldsymbol{J}(\boldsymbol{r}_{Tm},\boldsymbol{r}) = \sigma(\boldsymbol{r})\boldsymbol{v}(\boldsymbol{r}_{Tm},\boldsymbol{r})\times\boldsymbol{B}$ is induced, with unit vector $\boldsymbol{e}_J$ perpendicular to $\boldsymbol{e}_v$.

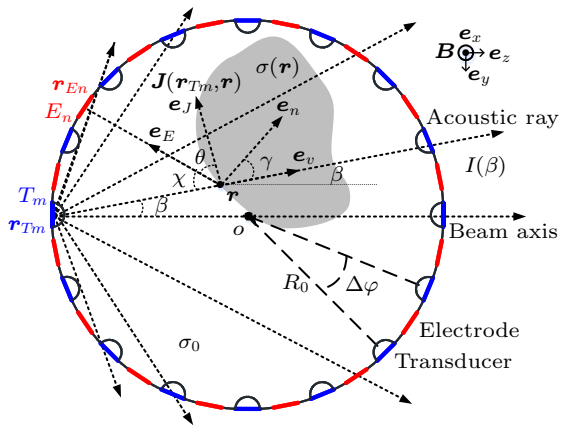


Fig. 1. Schematic diagram of rapid MAET utilizing circular arrays of omnidirectional transducers and electrodes.

The electrical potential detected by E_n at $\boldsymbol{r}_{En}$ is created by the component of $\boldsymbol{J}(\boldsymbol{r}_{Tm},\boldsymbol{r})$ along the direction of $\boldsymbol{r}\boldsymbol{r}_{En}$, which is described by $\boldsymbol{J}_{En}(\boldsymbol{r}_{Tm},\boldsymbol{r}) = \boldsymbol{J}(\boldsymbol{r}_{Tm},\boldsymbol{r})\cos\theta$. Here, θ is the angle between $\boldsymbol{e}_E$ and $\boldsymbol{e}_J$ with $\boldsymbol{e}_E = (\boldsymbol{r}_{En}-\boldsymbol{r})/|\boldsymbol{r}_{En}-\boldsymbol{r}|$. The MAE signal detected by E_n is determined by the equivalent resistance R_{En} along the current propagation path and the reception coefficient α of the electrodes. Thereby, by integrating over $\boldsymbol{r}$ within the field domain Ω, the MAE signal detected by E_n generated by T_m is given by

$$V(\boldsymbol{r}_{En},\boldsymbol{r}_{Tm},t) = \alpha B\iint_{\boldsymbol{r}\in\Omega} R_{En}\sigma(\boldsymbol{r})v(\boldsymbol{r}_{Tm},\boldsymbol{r})\cos\theta\,\mathrm{d}\boldsymbol{r}, \quad (2)$$

where $\theta = \pi/2-\chi$ with χ being the angle between $\boldsymbol{e}_E$ and $-\boldsymbol{e}_v$. For the acoustic wave $\exp(\mathrm{j}\omega t)$, the MAE signal can be revised through integration by parts

$$V(\boldsymbol{r}_{En},\boldsymbol{r}_{Tm},t) = -\frac{\alpha B}{\rho}\iint_{\boldsymbol{r}\in\Omega} R_{En}\frac{\partial\sigma(\boldsymbol{r})}{\partial\boldsymbol{e}_v} \times\left[\int_0^t p(\boldsymbol{r}_{Tm},\boldsymbol{r})\,\mathrm{d}t\cos\theta\right]\mathrm{d}\boldsymbol{r}. \quad (3)$$

Here $p(\boldsymbol{r}_{Tm},\boldsymbol{r})/(\mathrm{j}\omega) = \int_0^t p(\boldsymbol{r}_{Tm},\boldsymbol{r})\,\mathrm{d}t$. $\partial\sigma(\boldsymbol{r})/\partial\boldsymbol{e}_v$ can be calculated through $\partial\sigma(\boldsymbol{r})/(\partial\boldsymbol{e}_n)\cos\gamma$, with γ representing the angle between $\boldsymbol{e}_v$ and the inward normal direction $\boldsymbol{e}_n$ of the conductivity boundary. Moreover, since $|\boldsymbol{r}_{En}-\boldsymbol{r}|$ varies with $\boldsymbol{r}_{En}$, R_{En} can be approximated to $R_{En} = R_s|\boldsymbol{r}_{En}-\boldsymbol{r}|$, with R_s denoting the resistance per unit length. Thus, the MAE signal is revised to

$$V(\boldsymbol{r}_{En},\boldsymbol{r}_{Tm},t) = \xi\iint_{\boldsymbol{r}\in\Omega}\left[\frac{\partial\sigma(\boldsymbol{r})}{\partial\boldsymbol{e}_n}\cos\gamma\right]\frac{\exp\left[\mathrm{j}\left(\omega t-kR_{Tm}\right)\right]}{|\boldsymbol{r}-\boldsymbol{r}_{Tm}|} \times|\boldsymbol{r}_{En}-\boldsymbol{r}|\cos\theta\,\mathrm{d}\boldsymbol{r}, \quad (4)$$

where $\xi = -2\alpha B a^2 u_0 R_s$ is a constant determined by the structure and parameters of the system.

By substituting the time-varying acoustic excitation with an ideal Dirac delta signal, Eq. (4) is modified to

$$V_\delta(\boldsymbol{r}_{En},\boldsymbol{r}_{Tm},t) = \xi\iint_{\boldsymbol{r}\in\Omega}\frac{\partial\sigma(\boldsymbol{r})}{\partial\boldsymbol{e}_n}\frac{|\boldsymbol{r}_{En}-\boldsymbol{r}|}{|\boldsymbol{r}-\boldsymbol{r}_{Tm}|} \times\cos\gamma\cos\theta\cdot\delta\left(t-|\boldsymbol{r}-\boldsymbol{r}_{Tm}|/c\right)\mathrm{d}\boldsymbol{r}. \quad (5)$$

Here, $V_\delta(\boldsymbol{r}_{En},\boldsymbol{r}_{Tm},t)$ is the spatial transfer function of the system, decided by $\boldsymbol{r}_{Tm}$, $\boldsymbol{r}_{En}$, and $\sigma(\boldsymbol{r})$. This confirms that MAE signals can only be generated at conductivity boundaries, with their amplitude determined by $\partial\sigma(\boldsymbol{r})/\partial\boldsymbol{e}_n$ and $\cos\gamma\cos\theta$.

By further considering the excitation waveform $S(t)$ and the impulse response $R(t)$ of each acoustic source, the temporal transfer function $R(t)\otimes S(t)$ is obtained, with $\otimes$ representing the convolution operation. Therefore, the MAE waveform collected by E_n under the excitation of T_m is obtained as

$$W(\boldsymbol{r}_{En},\boldsymbol{r}_{Tm},t) = V_\delta(\boldsymbol{r}_{En},\boldsymbol{r}_{Tm},t)\otimes[R(t)\otimes S(t)]. \quad (6)$$

It reveals that each MAE waveform resolves into clusters whose pattern is dictated by the specific temporal transfer function of the transducers.

Leveraging the $M \times N$ MAE waveforms acquired through cyclic excitation and synchronous detection, an advanced reconstruction algorithm for MAET is developed. Firstly, by applying the Hilbert transform, the signal envelope of each MAE waveform is extracted through $H(\boldsymbol{r}_{En}, \boldsymbol{r}_{Tm}, t) = \mathrm{ABS}\left(\mathrm{Hilbert}\left[W(\boldsymbol{r}_{En}, \boldsymbol{r}_{Tm}, t)\right]\right)$. Then, invoking an inverse Radon transform for diffractive acoustic radiation, a B-mode MAE image is reconstructed by back-projecting each envelope amplitude onto the arc centered at $\boldsymbol{r}_{Tm}$ with a radius of ct. Finally, the image intensity is recovered by

$$g\left(\boldsymbol{r}_{En}, \boldsymbol{r}_{Tm}, \boldsymbol{r}\right) = H\left(\boldsymbol{r}_{En}, \boldsymbol{r}_{Tm}, t\right) \delta\left(R_{Tm} - ct\right), \tag{7}$$

where $\delta\left(R_{Tm} - ct\right)$ transforms the time-varying amplitude into a spatial distribution.

The MAE signal generated by the tissue boundary at $\boldsymbol{r}$ varies with $\boldsymbol{r}_{En}$, following a cosine function with respect to the angle θ. This issue can be solved by synchronously collecting MAE signals using N uniformly distributed electrodes. The signal attenuation can be effectively mitigated through the amplitude summation of the N envelopes, thereby enhancing the accuracy of the signal amplitude. Consequently, the B-mode image corresponding to the excitation source T_m and the synchronous detection using N electrodes is obtained by

$$g\left(\boldsymbol{r}_{Tm}, \boldsymbol{r}\right) = \sum_{n=1}^{N} g\left(\boldsymbol{r}_{En}, \boldsymbol{r}_{Tm}, \boldsymbol{r}\right). \tag{8}$$

Since the MAE signal also follows a cosine function[35] with respect to the angle γ, achieving accurate B-mode imaging for tissue boundaries based on a single acoustic excitation remains challenging. This issue can be addressed by cyclically exciting M sources and synchronously detecting signals using N electrodes. This approach enables us to recover M B-mode images from the collected $M \times N$ waveforms. Thus, by further applying the rotation matrix,[32] the MAET image can be reconstructed by

$$g\left(\boldsymbol{r}\right) = \sum_{m=1}^{M} \begin{pmatrix} \cos(m\Delta\phi) & \sin(m\Delta\phi) \\ -\sin(m\Delta\phi) & \cos(m\Delta\phi) \end{pmatrix} g\left(\boldsymbol{r}_{Tm}, \boldsymbol{r}\right). \tag{9}$$

Therefore, to ensure the accuracy of MAET imaging for objects of arbitrary shapes, a sufficient number of sources and electrodes uniformly distributed around a circumference are necessary to mitigate the signal attenuation caused by the angles θ and γ. The image quality can be enhanced by increasing the values of M and N. However, it is still influenced by the possible pressure difference of transducers and the strengthened acoustic reflection and scattering caused by electrodes. Therefore, it is crucial to optimize the system with fewest possible transducers and electrodes to enhance the efficiency of MAET imaging while maintaining high quality.

3. Numerical simulations

A MAET system with 16 sources and 16 electrodes was established, operating at a frequency of 2 MHz. The cross-sectional layout in the yz plane is illustrated in Fig. 2(a). Sixteen omnidirectional transducers and sixteen needle electrodes are evenly and alternately positioned on the circumference with a radius of 40 mm, centered at the origin. A cylindrical tissue model with a radius of 10 mm is eccentrically positioned within the field domain, with its center located at (10, 10) mm. The electrical conductivities of the model and the surrounding water are set to 1 S/m and 0.1 S/m, respectively. The sound speeds in both the model and water are set to 1450 m/s. Acoustic scattering and reflection across the entire field domain are disregarded. By cyclically exciting the 16 sources using the Dirac delta signal and synchronously detecting electrical potentials with the 16 electrodes, a total of 16×16 MAE signals are simulated. As indicated by the dashed arcs in Fig. 2(a), the wavefronts originating from sources T_3 and T_{16} propagate along their respective beam axes in a hemispherical radiation pattern. The intersections A and B, as well as C and D, situated on the front and back boundaries, are specifically labeled with white crosses ($\times$).

Taking the excitation source T_3 as an example, the MAE signals detected by E_3 and E_{11} were simulated, as presented in Fig. 2(b). The MAE signal excited by T_{16} and detected by E_{11} is also provided for comparison. All signals display two distinct pulses, with abrupt changes occurring at times that precisely match the propagation distances from the sources to the boundaries A and B, as well as C and D. The positive and negative values of the pulses reflect the opposite polarities of the conductivity gradients along their respective propagation directions. When excited by T_3, the pulse positions of the two MAE signals detected by E_3 and E_{11} are exactly identical, as they share the same propagation path. The peaks of pulses A and B, which are located at 21.2 μs and 34.8 μs, respectively, correspond to the intersections A and B on the front and rear boundaries. The corresponding propagation distances of approximately 30.7 mm and 50.4 mm, with a difference of 19.7 mm, are in excellent agreement with the acoustic transmission within the model. For the detection by an electrode, the MAE signal attenuates with the angle γ and forms a gradually decreasing distribution from the positive peak to the negative one, with the zero point occurring at the boundary with $\gamma = 90^\circ$. However, for the same excitation source, the MAE signals detected by different electrodes exhibit varying amplitudes due to the different values of R_{En} and θ. Consequently, the positive and negative pulse peaks detected by E_3 are significantly lower than those detected by E_{11}, as shown in Fig. 2(b). Additionally, when the excitation is switched to T_{16}, the two pulses detected by E_{11} are markedly different from those ex-

cited by T_3 in both amplitude and time. This discrepancy stems from the different positions of the front and rear boundaries for different excitations.

These findings demonstrate that the MAE signal is highly dependent on the positions of the source and electrode, further validating the mechanism of signal attenuation for inclined conductivity boundaries.[35] Therefore, the signal attenuation caused by the electrode position can be effectively mitigated by employing synchronous detection using multiple electrodes evenly arranged along the circumference. By leveraging the more accurate information within the field domain offered by MAE signals, the image quality for conductivity boundaries can be significantly enhanced. Consequently, by integrating the impulse response with a single-cycle sinusoidal excitation of the transducers, 16×16 MAE waveforms were simulated through convolution. Three waveforms corresponding to the MAE signals in Fig. 2(b) are depicted in Fig. 2(c). Four distinct clusters corresponding to the respective conductivity boundaries are clearly visible, with their positions and amplitudes determined by the pulses in Fig. 2(b). Consequently, the envelopes of the MAE waveforms were computed using the Hilbert transform, as illustrated in Fig. 2(d). These distributions display four peaks, with their positions, heights, and widths being determined respectively by the positions and amplitudes of the abrupt changes, as well as the shape of the temporal transfer function.

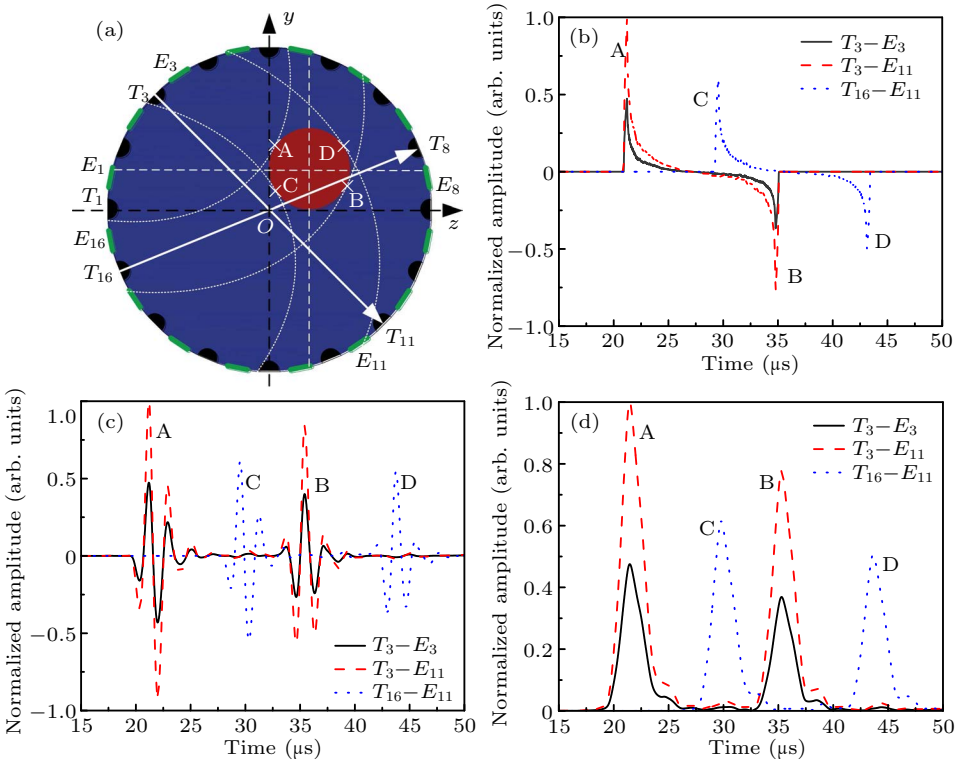


Fig. 2. (a) Schematic illustration of a MAET system utilizing 16 transducers and 16 electrodes, with an eccentrically positioned cylindrical tissue model. (b) Simulated MAE signals generated by the source and electrode at different positions, (c) collected MAE waveforms and (d) corresponding envelopes obtained via Hilbert transform.

Using the MAE envelope $H(\boldsymbol{r}_{E11}, \boldsymbol{r}_{T3}, t)$, the B-mode image $g(\boldsymbol{r}_{E11}, \boldsymbol{r}_{T3}, \boldsymbol{r})$ corresponding to T_3 and E_{11} was initially reconstructed by applying Eq. (7), as depicted in Fig. 3(a). Two arcs are visualized, with their radii representing the transmission distances from $\boldsymbol{r}_{T3}$ to the left and right model boundaries A and B. Owing to the higher amplitude of the front peak in Fig. 2(d), the intensity of the left arc is significantly higher than that of the right one. To mitigate the influence of electrode positioning, sixteen envelopes $H(\boldsymbol{r}_{En}, \boldsymbol{r}_{T3}, t)$, synchronously collected by 16 electrodes under the excitation of T_3, are utilized to recover $g(\boldsymbol{r}_{T3}, \boldsymbol{r})$ using Eq. (8) via amplitude summation. The resulting image in Fig. 3(b) presents double arcs whose shape closely resembles that in Fig. 3(a). The weaker intensity of the right boundary is greatly enhanced through the amplitude summation for the 16 MAE waveforms. However, due to the pressure attenuation during acoustic transmission, the intensity of the right arc remains lower than that of the left one. By leveraging the 16×16 envelopes $H(\boldsymbol{r}_{En}, \boldsymbol{r}_{Tm}, t)$, sixteen B-mode images $g(\boldsymbol{r}_{Tn}, \boldsymbol{r})$ corresponding to the 16 sources were reconstructed. The MAET image $g(\boldsymbol{r})$ was finally recovered by introducing the rotation matrix with $\Delta\phi = \pi/8$ using Eq. (9). As shown in Fig. 3(c), the resultant image clearly displays an annulus centered at (10, 10) mm with a radius of 10 mm, which is fundamentally consistent with the boundary configuration of the model. Nevertheless, due to the limited number of sources, the continuity and smoothness of the annulus are markedly compromised in both shape and intensity, leading to distinct

external artifacts.

To determine the minimum number of transducers required for MAET system, the impact of the source number on imaging quality was investigated. As illustrated in Fig. 4(a), a cylindrical tissue model with a radius of 10 mm and a conductivity of 1 S/m is immersed in water, centered at the origin. M sources are evenly placed along the circumference with a radius of 40 mm, and 16 electrodes are uniformly arranged to detect the MAE signals. $M \times 16$ MAE waveforms are utilized to reconstruct MAET images. These resultant images are depicted in Figs. 4(b1)–4(b5) for $M = 10$, 15, 20, 30, and 40, respectively. Each image displays an annulus centered at the origin, with the intensity peak situated on the ring with a radius of 10 mm. The results confirm that the annular boundary can be reliably reconstructed with 16 electrodes ($N = 16$), exhibiting improved reconstruction quality with an increased number of sources.

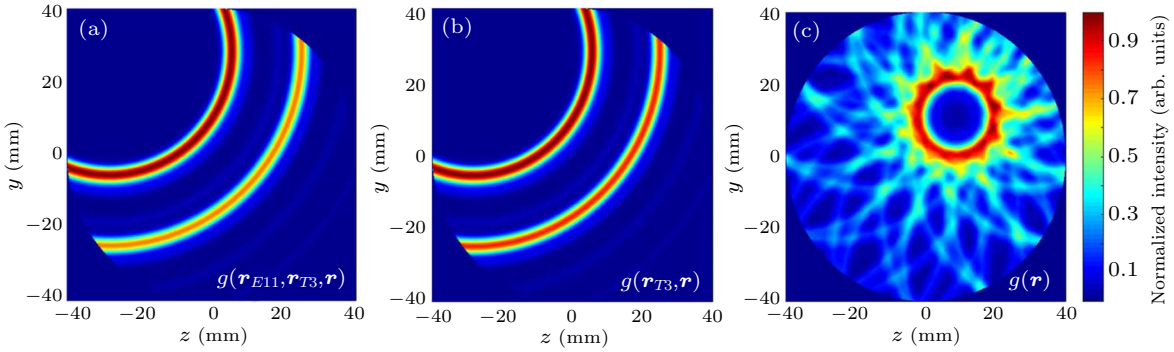


Fig. 3. B-mode images recovered with the MAE waveforms detected by (a) E_{11} and (b) 16 electrodes, under the excitation of T_3, (c) MAET image reconstructed with cyclic excitation of 16 sources and synchronous detection by 16 electrodes.

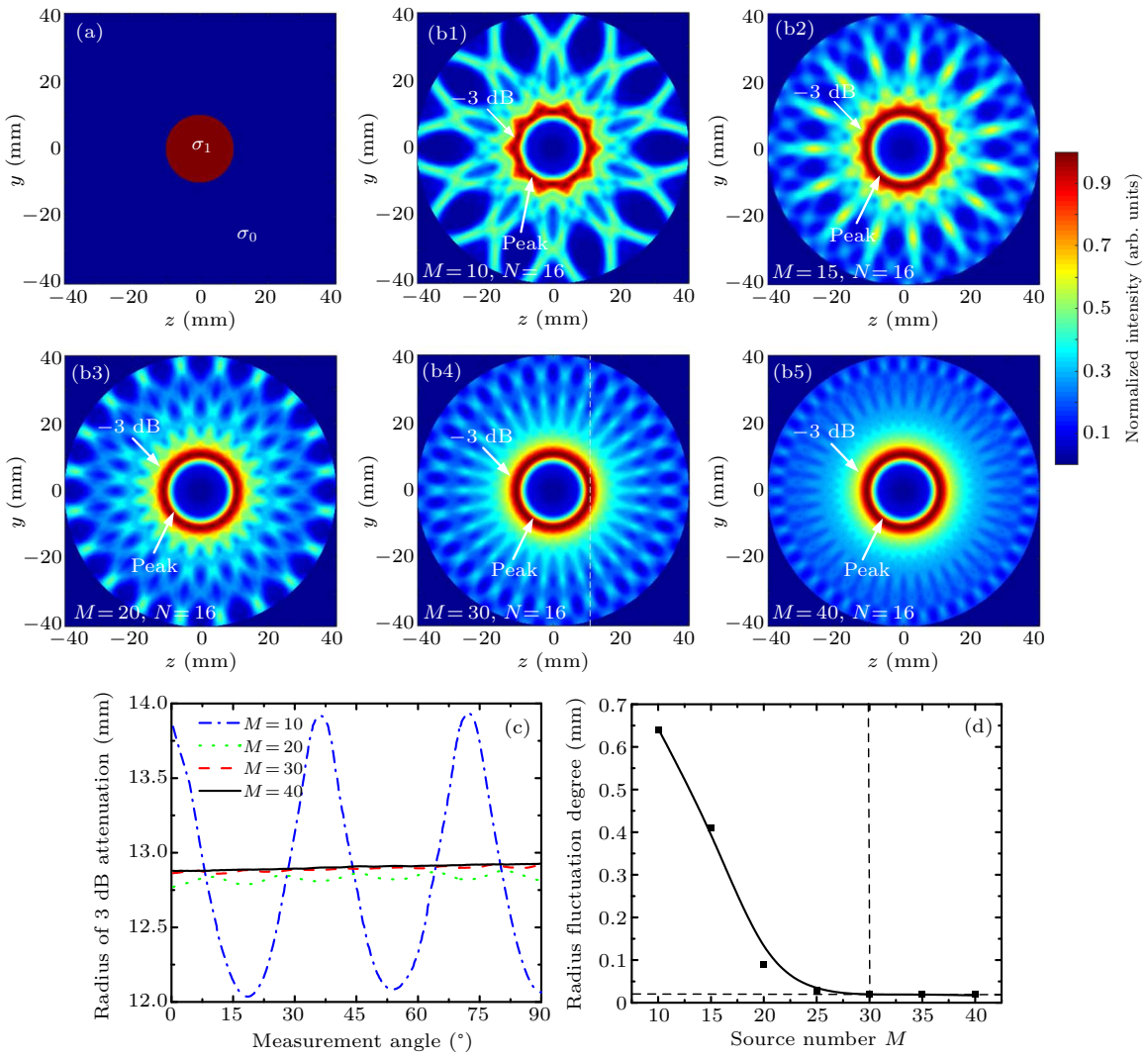


Fig. 4. (a) Cross-sectional conductivity map of the cylindrical model, reconstructed MAET images for $M =$ (b1) 10, (b2) 15, (b3) 20, (b4) 30, and (b5) 40 with $N = 16$, (c) circular distributions of the boundary radius for different source numbers, and (d) the source number dependence of the radius fluctuation degree.

To assess the quality of the reconstructed boundary, the iso-amplitude curves corresponding to 3 dB attenuation were extracted from the images shown in Figs. 4(b1)–4(b5). The circular distributions of the outer radius (R_{-3}) associated with 3 dB fall within the range from 0° to 90° are depicted in Fig. 4(c). These plots reveal pronounced radius fluctuations along the circumference, with the fluctuation range diminishing as M increases. To evaluate the smoothness and continuity of the circular boundary, the radius fluctuation degree is defined as

$$\varepsilon = \sqrt{\sum_{i=1}^{Q} \left[R_{-3}(i) - \overline{R_{-3}}\right]^2 / (Q-1)}, \tag{10}$$

where $R_{-3}(i)$ is the radius at the i-th sampling angle, and $\overline{R_{-3}}$ is the average over the Q sampling angles around the annulus. The distribution of the radius fluctuation degree as a function of the source number is plotted in Fig. 4(d). The results show that the fluctuation degree decreases from 0.64 mm to 0.019 mm as M increases from 10 to 40, indicating that a larger source number results in weaker fluctuations. Taking $\varepsilon = 0.02$ mm as the criterion, the minimum source number required for MAET system is $M = 30$. This result is well consistent with the conclusion that a maximum rotation angle of 12°[35] should be employed using the linear array of point sources.

Further investigations were conducted to explore the impact of the number and positions of electrodes on MAET imaging. A MAET system was established using 30 transducers in conjunction with 64 electrodes, with the sources and electrodes uniformly distributed along the circumference. A cylindrical model was immersed in water and centered at (10, 10) mm, as shown in Fig. 2(a). By selecting N electrodes evenly around the circumference, electrode combinations of $N = 1$, 2, 4, 8, 16, 32, and 64 were formed to conduct synchronous measurements, with the difference in numbering between adjacent electrodes being $64/N$. For the first electrode number indexed by n_s, the number of the i-th electrode is given by mod $(n_s + 64i/N, 64)$, $i = 0$ to $N-1$, where mod(X, Y) calculates the remainder of X divided by Y. With 30 cyclic excitations, MAET images for different n_s values were reconstructed, as presented in Figs. 5(a), 5(b), and 5(c) for $N = 1$, 2, and 4, respectively. The recovered images shown in Figs. 5(a1), 5(a2), and 5(a3), corresponding to $N = 1$ with $n_s = 8$, 27, and 54, respectively, reveal that the annular boundary can be essentially reconstructed using a single electrode positioned at different locations. Nevertheless, significant differences in annular intensity are still evident. As shown in Fig. 5(a1) for $n_s = 8$, the intensity peak of the annular boundary is situated near E_8, while the intensity valley lies in the opposite direction. The significant intensity difference produces an approximately discontinuous boundary distribution, thereby confirming that the intensity consistency and continuity of MAET imaging are severely impacted by the specific positions of the electrodes.

By increasing N to 2, MAET images reconstructed with two symmetrically arranged electrodes ($E_8 + E_{40}$, $E_{27} + E_{59}$, and $E_{54} + E_{22}$) are depicted in Figs. 5(b1), 5(b2), and 5(b3) for $n_s = 8$, 27, and 54, respectively. These images show that the intensity difference is significantly reduced, thereby improving the intensity consistency of the annular boundary. However, distinct intensity differences caused by the electrode positions remain evident. Furthermore, the MAET images recovered with 4 orthogonally positioned electrodes ($E_8 + E_{24} + E_{40} + E_{56}$, $E_{27} + E_{43} + E_{59} + E_{11}$, and $E_{54} + E_6 + E_{22} + E_{38}$) are presented in Figs. 5(c1), 5(c2), and 5(c3), respectively. The resultant images for $n_s = 8$, 27, and 54 exhibit nearly identical annular boundaries, with minimal perceptible variations in both intensity and position. The results demonstrate that MAE measurements using 4 orthogonally oriented electrodes can effectively enhance the accuracy of MAET imaging by improving the information integrity of MAE signals. Additionally, the imaging quality remains largely invariant with respect to the specific positions of 4 electrodes.

To evaluate the quality of MAET imaging, the relative error (RE) of the reconstructed annular boundary is employed

$$\mathrm{RE} = \sqrt{\sum_{i=1}^{Q} \left[g_p(i) - g_0\right]^2 / Q}, \tag{11}$$

where g_0 denotes the boundary intensity, normalized to 1 for the model. Q is the total sampling number around the annular boundary, and $g_p(i)$ is the intensity at the i-th sampling angle, normalized by the intensity peak. The RE values calculated from Figs. 5(a), 5(b), and 5(c) for $n_s = 8$, 27, and 54 are approximately 0.18, 0.24, and 0.13 for $N = 1$; 0.07, 0.17, and 0.16 for $N = 2$; 0.027, 0.027, and 0.027 for $N = 4$, respectively. It is evident that the RE values for $N = 1$ and 2 are relatively larger, exhibiting significant variations with the positions of the electrodes. In contrast, the RE values achieved by 4 orthogonally positioned electrodes are all decreased to 0.027, nearly unaffected by the specific positions of the electrodes.

MAET images were further reconstructed by varying n_s from 1 to 64 for $N = 1$, 2, 4, 8, 16, and 32, and the corresponding RE distributions as a function of n_s are plotted in Fig. 5(d). Each RE distribution exhibits periodic fluctuations with a period of N, and the amplitude of these fluctuations decreases as N increases. For $N = 1$ and 2, the RE distributions show relatively larger fluctuation ranges, indicating that the electrode positions have a substantial impact on image quality. In contrast, the RE decreases rapidly to 0.027 when $N \geq 4$ with minimal fluctuations. This verifies that using multiple groups of 4 orthogonally oriented electrodes along the circumference can significantly improve the quality of MAET imaging, making it almost independent of the specific positions of the electrodes.

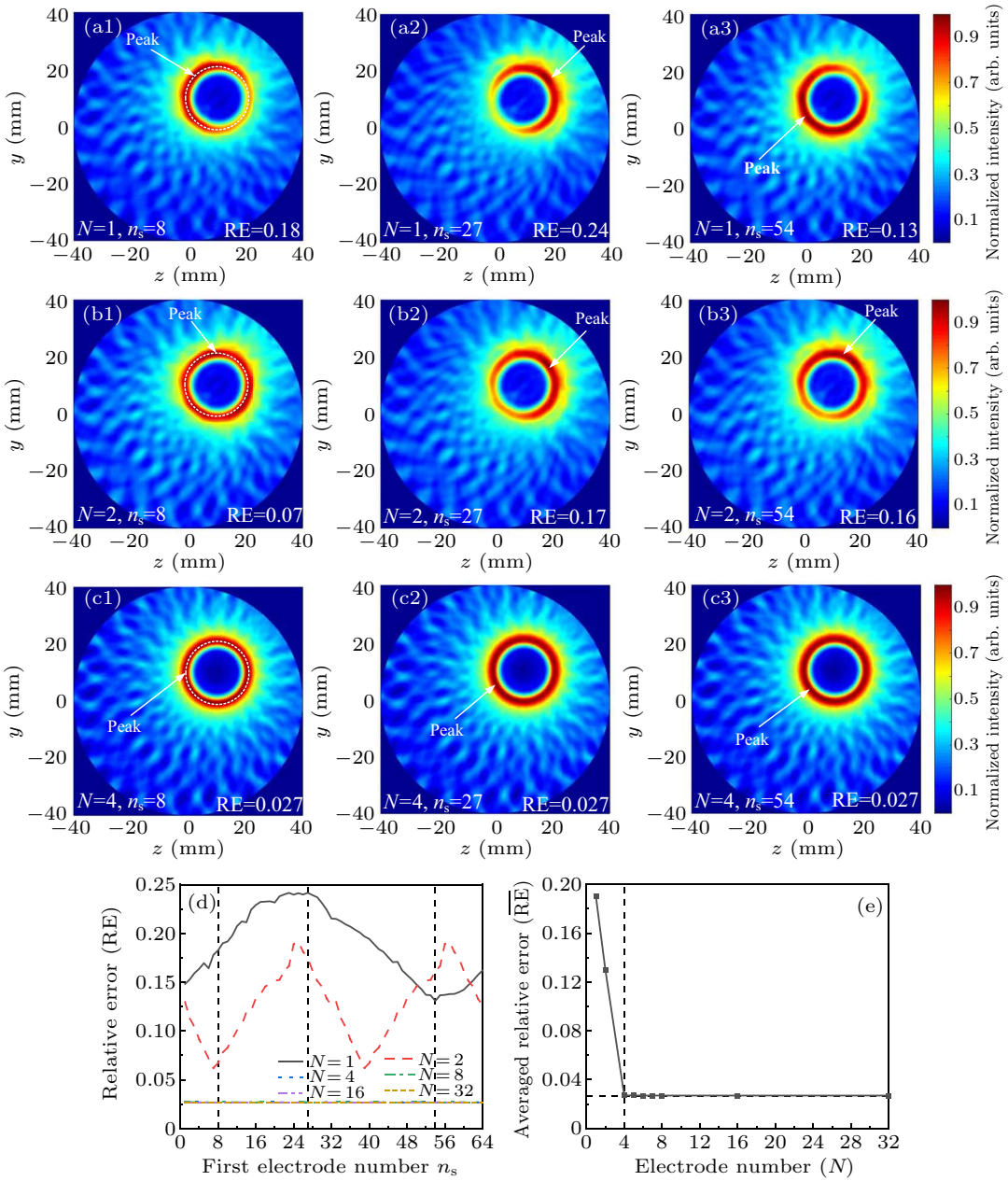


Fig. 5. MAET images for $M = 30$ and $N =$ (a1, a2, a3) 1, (b1, b2, b3) 2, and (c1, c2, c3) 4 with $n_s =$ (a1, b1, c1) 8, (a2, b2, c2) 27, and (a3, b3, c3) 54. (d) Relative error distributions of MAET images with respect to ns for various N values, and (e) the electrode number dependence of the averaged RE.

Furthermore, for non-orthogonal distributions, simulations were conducted with 5, 6, and 7 electrodes evenly spaced along the circumference under the condition of 30 acoustic sources. The reconstructed images of the annular boundaries coincide well with those in Figs. 5(c1), 5(c2), and 5(c3) in terms of shape, size and position. The RE values for$N = 5$, 6, and 7 are consistently around 0.027, which are comparable to the results obtained with 4 orthogonally oriented electrodes. These findings further confirm that for non-orthogonal circular distributions of electrodes, clear and accurate boundary images can be reconstructed when $N \geq 4$. Moreover, the image quality is basically not significantly improved by further increasing the number of electrodes. Additionally, by calculating the arithmetic mean of RE distribution for each N, the dependence of the averaged RE on the electrode number was achieved, as plotted in Fig. 5(e). This curve shows that the averaged RE decreases rapidly from 0.19 to 0.027 as N increases from 1 to 4, and it tends to stabilize at a similar value when $N > 4$. These results indicate that the image quality is relatively poor when $N < 4$. In contrast, the accuracy of MAE signals can be adequately enhanced by using 4 orthogonally oriented electrodes, and it cannot be further significantly enhanced by using more combinations of 4 orthogonally positioned electrodes. Therefore, by balancing the quality, efficiency, and stability of MAET imaging, the minimal configuration of the system is demonstrated to be $M = 30$ and $N = 4$. Furthermore, considering the practical requirements for uniform transducer arrangement and orthogonally oriented electrodes around a circumference, the minimized configuration of the MAET system can be optimized to $M = 32$ and $N = 4$.

4. Experimental demonstration

As is well known, the specific radiation pattern of a regular planar piston transducer is determined by the product of the wave number k and the radius a. Although the ideal omnidirectional acoustic radiation can be generated by a transducer with $ka \ll 1$ [36] or the acoustic transmission via an infinitesimal aperture, the resulting pressure is too low to be practical for MAET imaging. To address this issue, the transducer with $a = 3.5$ mm and $f = 2$ MHz was used as the acoustic source. A hemispherical convex acoustic lens, with the radius matching that of the transducer, was designed and fabricated using acrylic resin (density 1270 kg/m^3, sound speed 2440 m/s). As shown in Fig. 6, each lens was coaxially mounted onto the transducer's surface to modulate the directions of acoustic waves, thereby creating an approximate omnidirectional field that mimics the radiation of a point source.

As depicted in Fig. 6, an experimental system composed of 32 transducers and 4 orthogonally positioned silver needle electrodes was established to demonstrate the feasibility of fast MAET imaging. These sources were uniformly installed along the circular boundary in the center plane of a cylindrical container, which had a diameter of 120 mm and a height of 40 mm. Acoustic waves emitted from the sources propagated radially along their respective beam axes. To minimize acoustic reflections, acoustic-absorbing materials were placed on the inner surface and bottom of the container. A cylindrical gel model with a diameter of 30 mm and a conductivity of 1.0 S/m was eccentrically placed within the container, which was filled with saline water with a conductivity of about 0.3 S/m to ensure optimal acoustic coupling and electrical transmission. The transducer surfaces and acoustic lenses were fully insulated from the surrounding saline water to minimize the interference between the acoustic and electric fields. The entire system was placed in the central region of a pair of NdFeB magnets (100 mm×100 mm×50 mm), which generated an approximately uniform magnetic field with a strength of about 0.3 T, fully covering the gel model.

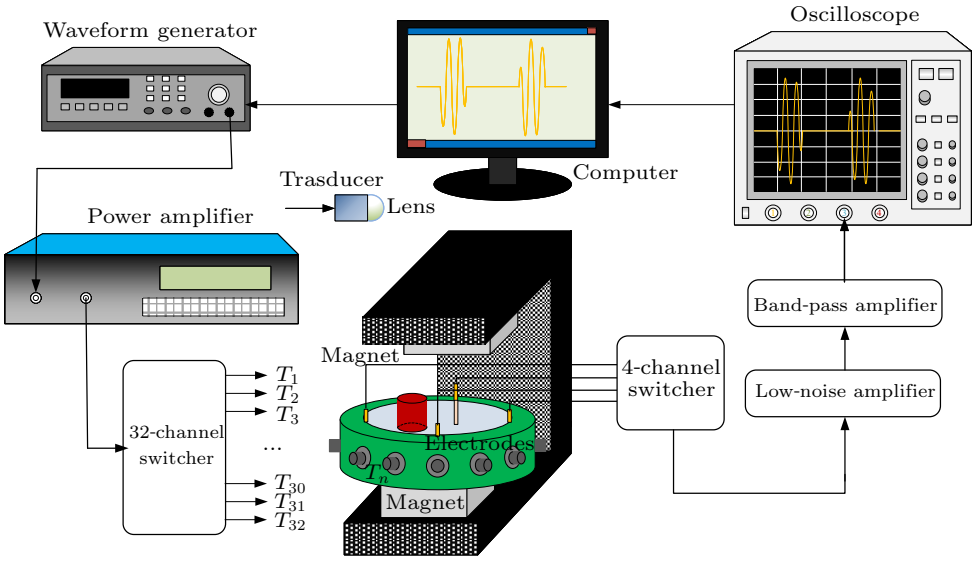


Fig. 6. Sketch map of the experimental MAET system consisting of 32 transducers and 4 orthogonally oriented needle electrodes.

Under the control of a computer, a single-cycle tone-burst waveform with a peak-to-peak voltage of 1 V, a frequency of 2 MHz, and a pulse repetition frequency of 100 Hz was sent out by a function generator (33220A, Agilent Technologies, USA). This signal was subsequently amplified by a power amplifier (53 dB, E&I 2200L, Electronics and Innovation Ltd., USA). Finally, the amplified signal was routed through a 32-channel switcher to drive the 32 transducers either individually or cyclically, thereby generating pulsed omnidirectional acoustic beams in the field domain. Four electrodes were orthogonally positioned on the inner side of the acoustic-absorbing materials to detect MAE signals generated at the conductivity boundaries of the model. These MAE signals were cyclically directed by a 4-channel switcher, and then amplified by a low-noise pre-amplifier (46 dB, NF SA-230F5, NF Corporation, Japan) and a custom-made band-pass amplifier (45 dB, bandwidth 1.5–2.5 MHz). The amplified signals were ultimately acquired by a digital oscilloscope (DSO9064A, Agilent Technologies, USA) and stored in the computer for further signal processing and MAET imaging.

Through experimental measurements, 32×4 MAE waveforms were collected via the cyclic excitation of 32 transducers and the synchronous detection using 4 electrodes. The cross-sectional conductivity configuration of the experimental system is depicted in Fig. 7(a), with the measured sound speed of approximate 1590 m/s within the model. A representative MAE waveform collected by one of the electrodes is illustrated in Fig. 7(b). Two distinct MAE clusters, A and B,

with opposite polarities, are clearly displayed. These clusters correspond to the front and back boundaries of the gel model, where the conductivity changes occur in opposite directions during acoustic propagation. Based on the envelope peaks A and B, the times of clusters A and B are determined to be 25.2 μs and 43.7 μs, respectively. The distance corresponding to the time interval (18.5 μs) between these two peaks matches well with the diameter (30 mm) of the model. In theoretical and numerical studies, the acoustic reflection and scattering at tissue boundaries are not taken into account. As a result, the wave clusters generated by tissue boundaries are distinctly visible in Fig. 2(b), free from any extraneous clutter. However, in experimental measurements, acoustic reflections at tissue boundaries, transducer lenses, and electrodes introduce several additional clusters with relatively lower amplitudes between clusters A and B, as observed in Fig. 7(b). These additional clusters may give rise to artifacts in MAET imaging.

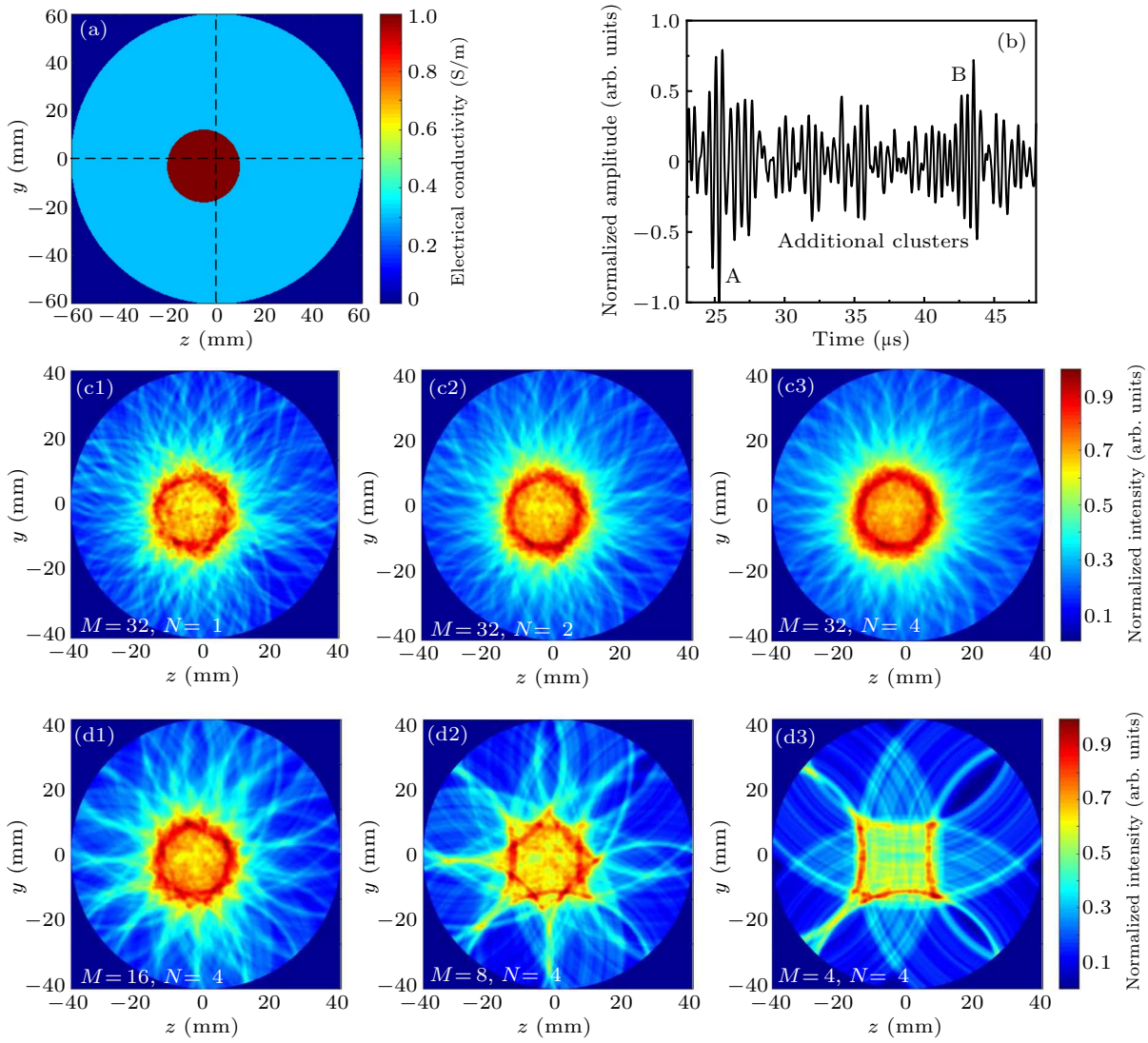


Fig. 7. (a) Cross-sectional conductivity map of the experimental configuration featuring an eccentrically positioned cylindrical gel model. (b) A MAE waveform collected by one electrode, MAET images reconstructed with $M = 32$ for $N =$ (c1) 1, (c2) 2, and (c3) 4, and with $N = 4$ for $M =$ (d1) 16, (d2) 8, and (d3) 4.

MAET images recovered with $M = 32$ are plotted in Figs. 7(c1), 7(c2), and 7(d3) for $N = 1$, 2, and 4, respectively, normalized by their respective maximum intensities. These resultant images indicate that the shape and size of the annular boundary can be precisely reconstructed using 32 sources. Since a single electrode is only capable of detecting the component of MAE signals along a specific direction, the boundary information of the conductivity gradient is inaccurate. As a result, the intensity consistency of the annular boundary in Fig. 7(c1) for $N = 1$ is compromised, with noticeable artifacts at the boundary. Moreover, distinct artifacts with varying intensities inside the annulus, produced by the possible acoustic reflections, are also obvious. When N is increased to 2, the image quality of the annular boundary in Fig. 7(c2) is improved, with the inside artifacts being obviously weakened. As depicted in Fig. 7(c3) for $N = 4$, the annular boundary is significantly enhanced by more accurate MAE signals detected by the 4 orthogonally oriented electrodes, resulting in

good continuity and uniformity with greatly suppressed artifacts. However, disparities in the excitation efficiencies of the 32 transducers introduce non-uniform acoustic pressure, leaving residual intensity fluctuations along the annular boundary. Furthermore, by selecting M sources from the 32 sources at a numbering interval of $32/M$ and conducting synchronous detection using 4 electrodes randomly placed in an orthogonal manner, MAET images were reconstructed using the collected $M \times 4$ MAE waveforms. The recovered images for $M = 16$, 8, and 4 are presented in Figs. 7(d1), 7(d2), and 7(d3), respectively. Compared with the image in Fig. 7(c3) for $M = 32$, the continuity and consistency of the annular boundary deteriorate as M decreases, forming a regular polygon with M sharp-pointed tips. Specifically, the images in Figs. 7(d2) and 7(d3), corresponding to $M = 8$ and 4, respectively, appear as an octagon and a quadrilateral. These shapes are significantly different from the annular distribution.

The experimental results confirm that the capability of boundary reconstruction is primarily determined by the source number (M) of the MAET system. Specifically, a more precise boundary shape can be recovered by a greater M. Meanwhile, the intensity consistency and continuity of reconstructed boundaries are predominantly decided by the electrode number (N). Consequently, increasing the numbers of acoustic sources and electrodes can markedly enhance image quality while suppressing artifacts. However, for electrode sets with orthogonal distributions, the total electrode number is preferably a multiple of 4, with a minimum of 4. These findings thus validate the optimized, real-world configuration of 32 sources and 4 orthogonally oriented electrodes as a fast, robust MAET solution.

5. Discussion

Theoretical analysis and experimental measurement demonstrate that the signal attenuation detected by an electrode follows a specific product of cosine functions, which is influenced by the positions of the sources and electrodes, as well as the directions of conductivity boundaries. Consequently, the quality of B-mode imaging is significantly affected by the positions of electrodes, which in turn has a profound impact on MAET. While increasing the electrode number can improve the information accuracy and integrity of MAE signals detected from more directions, the MAET image reconstructed with the amplitude summation algorithm remains dependent on the specific positions of the electrodes. This variation may lead to noticeable intensity fluctuations along the boundaries. Therefore, the proper arrangement of electrodes to obtain more accurate MAE signals is of great significance to MAET.

The accuracy of MAE signals can be ensured by synchronously detecting the components via 4 orthogonally oriented electrodes. For an induced current with a constant density (normalized to 1) at $\boldsymbol{r}$ in the field domain, the intensity of B-mode imaging detected by a single electrode varies from 0 to 1. Consequently, the image intensity reconstructed via amplitude summation for MAE signals detected by 4 orthogonally oriented electrodes can be simplified to $(2|\cos\theta| + 2|\sin\theta|)/4$. Hence, the resulting intensity varies within the range [0.5, 0.707], and the specific maximum of 1 is only achieved when $\theta = 0$. This indicates that the image intensity still has potential fluctuations due to the positional rotation of the 4 orthogonally oriented electrodes. Further considering the relationship between the orthogonal components $\cos\theta$ and $\sin\theta$ detected by the 4 electrodes, the reconstruction algorithm is refined by employing square-amplitude summation

$$g(\boldsymbol{r}_{Tm}, \boldsymbol{r}) = \sqrt{\sum_{n=1}^{4} g^2(\boldsymbol{r}_{En}, \boldsymbol{r}_{Tm}, \boldsymbol{r})}/2. \tag{12}$$

Here, the image intensity at $\boldsymbol{r}$ remains a constant of 1, independent on the specific angles of the 4 orthogonally oriented electrodes. Therefore, the accuracy of MAET imaging can be greatly enhanced by employing the square-amplitude summation algorithm.

Simulations were conducted using a MAET system with $M = 30$ and $N = 4$ for the eccentrically positioned cylindrical model. MAET images recovered via square-amplitude summation are illustrated in Figs. 8(a1), 8(a2), and 8(a3) for $n_s = 8$, 27, and 54, respectively. These images are almost similar to those as depicted in Figs. 5(c1), 5(c2), and 5(c3). It is evident that the conductivity boundary of the model can be accurately recovered using both the amplitude summation and square-amplitude summation algorithms for MAE signals detected by the 4 orthogonally positioned electrodes. Subsequently, circular intensity distributions of the annular boundary reconstructed via square-amplitude summation were calculated for $n_s = 8$, 27, and 54, and are plotted in Fig. 8(b). The three curves are almost identical in both shape and intensity, with variations ranging from 0.955 to 0.995. This confirms that the MAET image recovered via square-amplitude summation for MAE signals detected by 4 orthogonally positioned electrodes is independent of the specific angles of electrodes. Furthermore, by varying n_s from 1 to 64, the circular RE distributions for the annular boundary reconstructed via both summation algorithms were achieved, as depicted in Fig. 8(c). The RE distribution achieved via amplitude summation exhibits periodic fluctuations confined to the range between 0.0266 and 0.0276. However, the RE curve obtained via square-amplitude summation is virtually independent of n_s, remaining steady between 0.02689 and 0.02692.

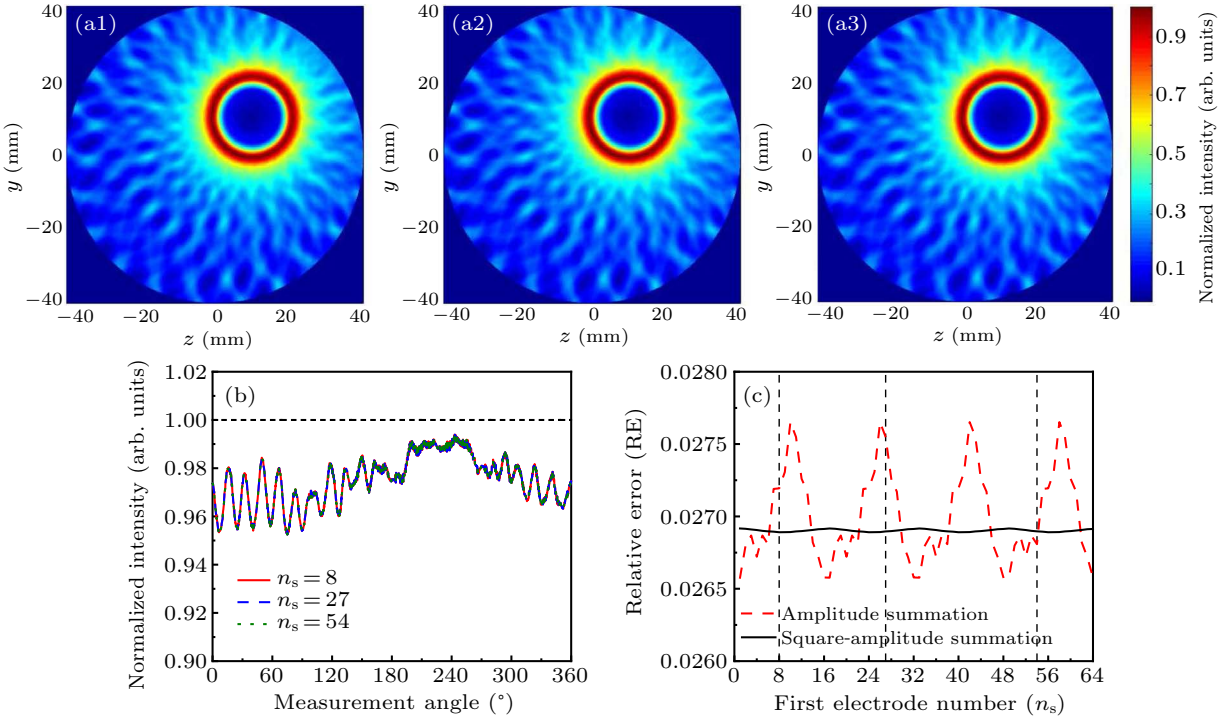


Fig. 8. MAET images reconstructed via square-amplitude summation for n_s = (a1) 8, (a2) 27, and (a3) 54 with $M = 30$ and $N = 4$, and (b) corresponding circular intensity distributions, (c) RE distributions of the annular boundary with respect to ns for images reconstructed via the amplitude summation and square-amplitude summation algorithms.

The simulation results indicate that the amplitude summation algorithm, derived from the conventional tomographic theory based on the inverse Radon transform in diffraction mode, is applicable to electrodes that are uniformly distributed around a circumference. The algorithm enables the reconstruction of a more accurate MAET image of conductivity boundaries as the number of electrodes increases, with a minimum of 4 electrodes. The amplitude summation algorithm meets the quality requirements. The advanced square-amplitude summation algorithm, distinguished by its clearer physical significance rooted in orthogonality, can significantly enhance the performance of MAET imaging. This unique characteristic makes it highly suitable for widespread applications in MAET, particularly when utilizing one or multiple sets of 4 orthogonally oriented electrodes. Notably, the square-amplitude summation algorithm is particularly suitable for the optimized system that employs 4 orthogonally placed electrodes.

Further simulations were conducted for cylindrical tissue models with different cross-sectional shapes, using circularly arranged 32 omnidirectional transducers and 4 orthogonally oriented electrodes. The reconstructed MAET images for the triangle, square, and ellipse boundaries, as plotted in Fig. 9, show good agreement with the models. Compared with the result reported by Sun *et al.*,[32] the ellipse-boundary image retains the same overall shape while exhibiting markedly superior continuity and consistency in pressure. These simulations demonstrate that the proposed MAET method is applicable to objects of arbitrary shapes and significantly improves imaging quality. Further accounting for the limited spatial resolution imposed by the transducers, state-of-the-art tomographic reconstruction algorithms, such as x-ray phase contrast imaging[37] and cross-waveband optical computing imaging,[38] can be embedded in MAET to markedly enhance image quality with an acceptable time cost.

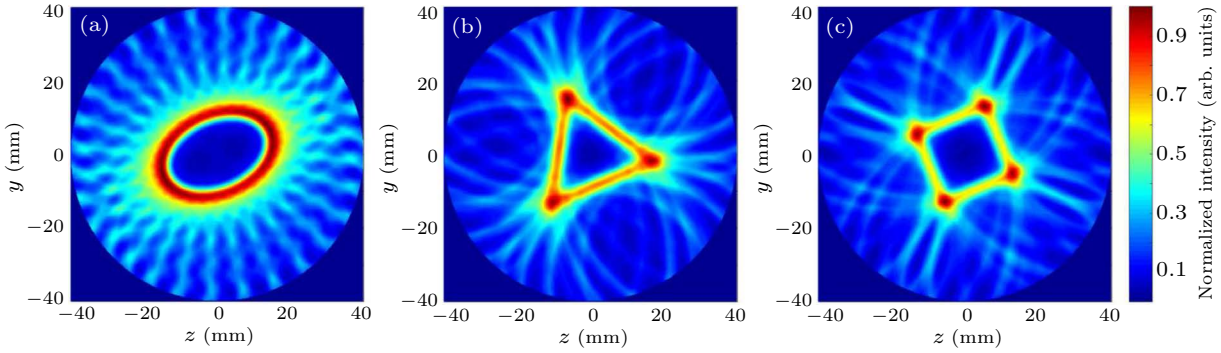


Fig. 9. Reconstructed MAET images for cylindrical tissue models with cross-sectional boundary shapes of (a) ellipse, (b) triangle, and (c) square.

6. Conclusion

To address the limitations in imaging accuracy and efficiency posed by mechanical rotation and scanning, an advanced MAET approach utilizing cyclic excitation of omnidirectional transducers and synchronous detection with orthogonally oriented electrodes is proposed. A general principle of MAE measurements is derived in an explicit formulation, which is applicable to acoustic excitation and electrode detection at any positions for objects of arbitrary shapes. The attenuation of MAE signals, which originates from the positions of excitation source and detection electrode, follows the cosine product of the angles between the conductivity boundary and the positions of the source and electrode. The information accuracy and integrity of MAE signals are enhanced through synchronous detection using more electrodes. The most pronounced improvement is achieved with 4 orthogonally arranged electrodes, independent of their specific positions. Consequently, a new MAET algorithm that employs amplitude summation for electrode detected signals is developed based on the inverse Radon transform. This algorithm is further refined by utilizing square-amplitude summation for MAE signals detected by 4 orthogonally oriented electrodes. To meet practical constraints regarding the circumferential placement of a minimum number of transducers and electrodes, the optimized configuration comprising 32 sources and 4 electrodes is validated both theoretically and experimentally. Because the acoustic beam emitted from an omnidirectional source can cover the entire object, the MAET system is free from the mechanical scanning or phased array steering. The efficiency and stability of MAET imaging are thus significantly improved by replacing mechanical rotation with electrically controlled cyclic excitation. Additionally, the proposed approach can be readily integrated into conventional ultrasonic CT, establishing a robust physical basis for dual-modality imaging that simultaneously leverages both electrical and acoustic impedances.

Acknowledgements

Project supported by the National Natural Science Foundation of China (Grant Nos. 12227808 and 12174198), the Natural Science Foundation of Jiangsu Province (Grant No. BE2022814), Qing Lan Project of Jiangsu Province, and Universal Technology for Primary and Secondary Schools, National Research Institute for Teaching Materials.

References

[1] Gabriel C, Gabriel S and Corthout E 1996 *Phys. Med. Biol.* **41** 2231
[2] Joines W T, Yang Z, Li C and Jirtle R L 1994 *Med. Phys.* **21** 547
[3] Wang H, He Y, Yang M, Yan Q, You F, Fu F, Wang T, Huo X, Dong X and Shi X 2014 *Biomed. Mater. Eng.* **24** 2725
[4] Prakash S, Karnes M P, Sequin E K, West J D, Hitchcock C L, Nichols S D, Bloomston M, Abdel-Misih S R, Schmidt C R and Martin Jr E W 2015 *Schmidt E. W. Martin Jr, Physiol. Meas.* **36** 315
[5] Grasland-Mongrain P and Lafon C 2018 *IRBM* **39** 243
[6] Ganesan A and Durgamahanthi V 2023 *Trait. Signal* **40** 2809
[7] Liu D, Smyl D and Du J 2020 *IEEE Trans. Instrum. Meas.* **69** 1894
[8] Griffiths H 2021 *Meas. Sci. Technol.* **12** 1126
[9] Chen R, Huang J, Li B, Wang J and Wang H 2020 *Rev. Sci. Instrum.* **91** 091501
[10] Soleimani M and Lionheart W R B 2006 *IEEE Trans. Med. Imag.* **25** 1521
[11] Kim H J, Kim Y T, Minhas A S, Jeong W C, Woo E J and Seo J K 2009 *IEEE Trans. Med. Imag.* **28** 1681
[12] Woo E J and Seo J K 2008 *Physiol. Meas.* **29** R1
[13] Song Y, Seo J K, Chauhan M, Indahlastari A, Kumar N A and Sadleir R 2018 *Phys. Med. Biol.* **63** 045011
[14] Wen H, Shah J and Balaban R S 1998 *IEEE Trans. Biomed. Eng.* **45** 119
[15] Haider S, Hrbek A and Xu Y 2008 *Physiol. Meas.* **29** S41
[16] Roth B J 2023 *Appl. Sci.* **13** 3877
[17] Li Y and Liu G 2023 *Chin. J. Electr. Eng.* **9** 47
[18] Grasland-Mongrain P, Destrempes F, Mari J M, Souchon R, Catheline S, Chapelon J Y, Lafon C and Cloutier G 2015 *Phys. Med. Biol.* **60** 3747
[19] Li Y, Liu G, Xia H and Xia Z 2018 *IEEE Trans. Magn.* **53** 5100704
[20] Li Y, Liu G, Sun Z, Xia H and Xia Z 2018 *J. Med. Imag. Health. Inf.* **8** 1402
[21] Zhou Y, Ma Q, Guo G, Tu J and Zhang D 2018 *IEEE Trans. Biomed. Eng.* **65** 1086
[22] Li Y, Song J, Xia H and Liu G 2020 *Phys. Med. Biol.* **65** 215024
[23] Yu Z, Zhou Y, Li Y, Ma Q, Guo G, Tu J and Zhang D 2018 *Chin. Phys. B* **27** 094302
[24] Zhang S, Zhou X, Liu S, Yin T and Liu Z 2018 *Biomed. Signal Process. Control* **39** 169
[25] Deng D, Sun T, Yu L, Chen Y, Chen X, Chen M, Chen S and Lin H 2022 *Biomed. Signal Process. Control* **77** 103823
[26] Dai M, Chen X, Sun T, Yu L, Chen M, Lin H and Chen S 2018 *Sensors* **18** 2373
[27] Zhang S, Mai W, Wang Y, Yin T and Liu Z 2022 *J. Mech. Med. Biol.* **22** 2240021
[28] Li M, Wang J, Jia K and Sun Z 2024 *Phys. Med. Biol.* **69** 215015
[29] Grasland-Mongrain P, Mari J M, Chapelo J Y and Lafom C 2013 *IRBM* **34** 357
[30] Kunyansky L, Ingram C P and Witte R S 2017 *Phys. Med. Biol.* **62** 3025
[31] Sun T, Zeng X, Hao P, Chin C T, Chen M, Yan J, Dai M, Lin H, Chen S and Chen X 2020 *Math. Biosci. Eng.* **17** 2864
[32] Sun T, Hao P, Chin C T, Deng D, Chen T, Chen Y, Chen M, Lin H, Lu M and Gao Y 2021 *Phys. Med. Biol.* **66** 095002
[33] Lin H, Chen Y, Yu L, Xie S, Sun T and Yu M 2023 *IEEE Trans. Biomed. Eng.* **70** 1493
[34] Sun T, Yu M, Yu L, Deng D, Chen M and Lin H 2024 *IEEE Trans. Biomed. Eng.* **71** 669
[35] Li P, Chen W, Guo G, Tu J, Zhang D and Ma Q 2023 *Med. Phys.* **50** 3076
[36] Cheng J 2020 *Principles of Acoustics* (Beijing: Science Press)
[37] Tan Y, Cai X, Yang J, Su T, Zhang H, Liang D, Zhu P and Ge Y 2024 *Chin. Phys. B* **33** 078702
[38] Xie J, Bie S, Li M, Yu Y, Li Y, Wang J, Quan B and Wu L 2024 *Chin. Phys. B* **33** 104203